Nanoscale

Revealing Inconsistencies in X-ray Width Methods for Nanomaterials

Journal:	*Nanoscale*
Manuscript ID	NR-ART-09-2019-008268.R1
Article Type:	Paper
Date Submitted by the Author:	05-Nov-2019
Complete List of Authors:	Kunka, Cody; Sandia National Laboratories Boyce, Brad; Sandia National Laboratories, Materials Science and Engineering Center Foiles, Stephen; Sandia National Laboratories Dingreville, Remi; Sandia National Laboratories, Nanostructure Physics

Revealing Inconsistencies in X-ray Width Methods for Nanomaterials

Cody Kunka,*,† Brad L. Boyce,*,† Stephen Foiles,*,‡ and Rémi Dingreville*,†

†*Center for Integrated Nanotechnologies, Sandia National Laboratories, Albuquerque, NM 87185, USA*

‡*Sandia National Laboratories, Albuquerque, NM 87185, USA*

E-mail: ckunka@sandia.gov; blboyce@sandia.gov; foiles@sandia.gov; rdingre@sandia.gov

Abstract

Since the landmark development of the Scherrer Method a century ago, multiple generations of width methods for X-ray diffraction originated to non-invasively and rapidly characterize the property-controlling sizes of nanoparticles, nanowires, and nanocrystalline materials. However, the predictive power of this approach suffers from inconsistencies among numerous methods and from misinterpretations of the results. Therefore, we systematically evaluated twenty-two width methods on a representative nanomaterial subjected to thermal and mechanical loads. To bypass experimental complications and enable a 1:1 comparison between ground truths and the results of width methods, we produced virtual X-ray diffractograms from atomistic simulations. These simulations realistically captured the trends that we observed in experimental synchrotron diffraction. To comprehensively survey the width methods and to guide future investigations, we introduced a consistent, descriptive nomenclature. Alarmingly, our results demonstrated that popular width methods, especially the Williamson-Hall Methods, can produce dramatically incorrect trends. We also showed that the simple Scherrer Methods and the rare Energy Methods can well characterize unloaded and loaded states, respectively. Overall, this work improved the utility of X-ray diffraction in experimentally evaluating a variety of nanomaterials by guiding the selection and interpretation of width methods.

Introduction

By correlating the broadening of peaks in X-ray diffraction (XRD) with material imperfections, width methods can non-invasively and rapidly track the characteristic, property-controlling sizes and microstrains of a wide range of nanomaterials[1,2] (*e.g.*, nanoparticles,[3,4] monocrystalline nanowires,[5,6] and nanocrystalline materials[7–9]). However, the predictive power of this approach suffers from inconsistencies among numerous methods and from misinterpretations of the results.

The many width methods employed today originated as modifications to the 1918 Scherrer Method, which attributed peak width (β) to a characteristic size (D).[10–12] Since that landmark publication, researchers have added new terms to represent the effects of other broadening sources.[13] In 1953, Williamson and Hall introduced a constant microstrain (ϵ) term.[14,15] This two-term method is the most popular approach today because it conveniently captures the effects of both size and strain without material-specific factors. However, ϵ is anisotropic by definition, so the Stress Methods, Energy Methods, and Dislocation Methods arose in the late 1990s and early 2000s. The Stress Methods and Energy Methods use the material-specific Young's moduli (E) to substitute ϵ for stress (σ) and deformation energy (u), respectively.[16] The Dislocation Methods instead use material-specific dislocation-contrast factors (C)[17,18] to represent ϵ by dislocation density (ρ) and sometimes also by dislocation correlation (Q).[19] These methods sometimes adjust D for for planar defects (P) as well.[20]

Further width methods arose by varying features other than the included broadening sources. First, every width method can incorporate different representations of β (*i.e.*, the width type).[21] For example, the original Scherrer Method assessed the full-width-half-max widths (F), which are the widths of the peaks at half of their amplitudes.[10] Eight years later, Laue introduced the most popular alternative: the integral-breadth widths (I), which are the areas of the peaks divided by their amplitudes.[22] Alongside width type, each multi-term model can vary in the way that the terms are convolved (*i.e.*, the functional forms). Williamson and Hall originally proposed two combinations: linear (*i.e.*, the convolution of Lorentzian functional forms) and quadratic (*i.e.*, the convolution of Gaussian functional forms). In 1966, Halder and Wagner introduced an intermediate approach by mixing a Lorentzian form with a Gaussian form.[23] This asymmetric approach was recently adapted into the Dislocation Methods[13,24] and the problematic Size-Strain-Plot Method,[25,26] which fails dimensional analysis.

Over time, the number of width methods grew exponentially with the introduction of new (1) broadening sources, (2) width types, and (3) functional forms. However, the nomen-

clatures for these emerging width methods did not evolve systematically. For example, width methods are commonly called "integral-breadth methods" even if F values are actually used. Likewise, because of the ubiquity of the Willliamson-Hall Method, which itself has multiple forms, newer methods (*e.g.*, Stress, Energy, and Dislocation Methods) frequently adopted the same name: "Modified Williamson-Hall Method." These overlapping nomenclatures invited researchers to incorrectly assume that all width methods produce the same trends in properties. Further, the traditional nomenclatures did not consistently define the characteristic size, which should represent the volume-averaged length of a column of coherently diffracting material (L).[7,21] Unfortunately, modern studies commonly failed to convert L to an equivalent domain diameter (D), to identify the difference between domain size and particle/nanowire/grain size, or to acknowledge the difference between the volume-averaged size from X-ray width methods and the area-averaged size from electron microscopy.[25,26]

To improve the utility of XRD in characterizing nanomaterials, we systematically evaluated the inconsistencies of twenty-two width methods. By using virtual XRD from atomistic simulations of a representative, nanocrystalline nanowire subjected to thermal and mechanical loads, we established a fully characterized ground truth for the microstructural evolution and avoided confounding factors intrinsic to diffraction experiments. These simulations realistically captured the trends that we observed in experimental synchrotron diffraction on a similar system. To survey the combinatorial space of width methods in this study and to facilitate future experimental studies, we presented a unified nomenclature, which explicitly denotes (1) broadening sources, (2) width type, and (3) functional forms. Our results revealed that all three elements can both quantitatively and qualitatively affect the resulting properties. Alarmingly, we showed that some popular Williamson-Hall Methods can produce dramatically incorrect trends. We also demonstrated that the simple Scherrer Methods and the rare Energy Methods can well characterize unloaded and loaded nanomaterials, respectively.

Results and Discussion

Synchrotron Diffraction

To evaluate the accuracies of the width methods without experimental complications (*e.g.*, broadening from instrumentation, uncertainty in composition, and limited access to three-dimensional crystallography), we employed atomistic simulations of nanocrystalline nickel (Ni) thermally and mechanically loaded at 500 K. To illustrate that these simulations were qualitatively realistic, we performed synchrotron diffraction of a nanocrystalline, nickel-iron

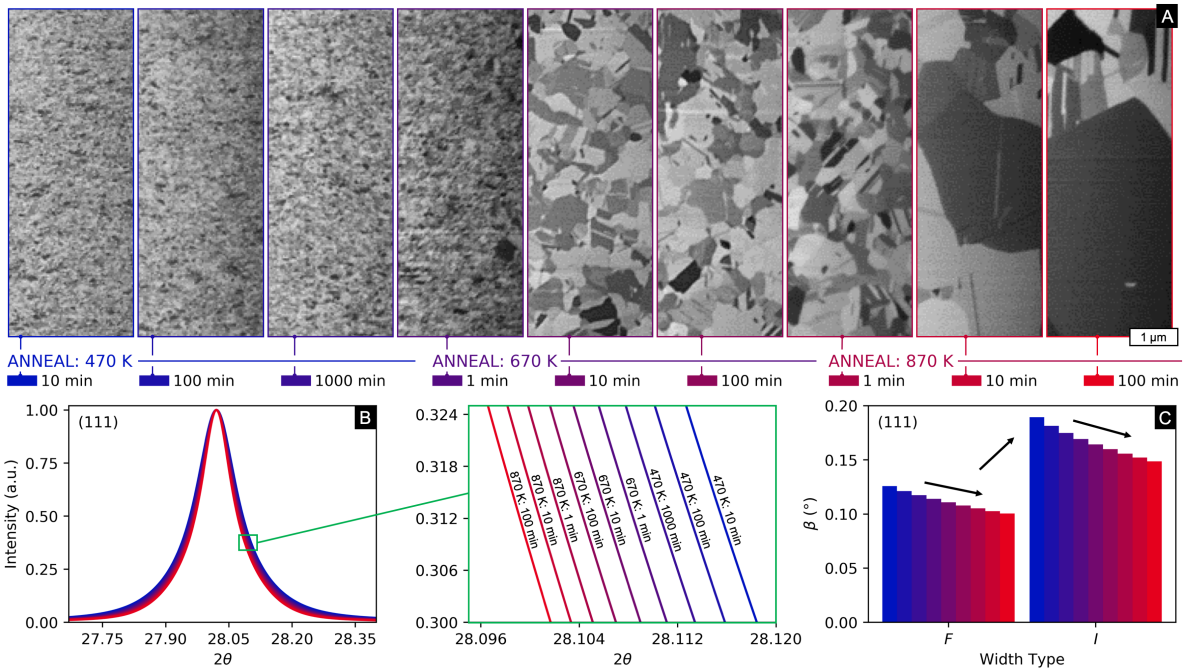

Figure 1. (A) Microstructures and (B) the (111) XRD peak for a nanocrystalline Ni-Fe alloy annealed at 470 K - 870 K. (C) The peak widths (β), which scale with width type (*i.e.*, F vs. I), cleanly reflect the grain growth apparent in the micrographs.

(Ni-Fe) alloy annealed at 470 K – 870 K.

Synchrotron diffraction comprehensively assesses the evolution of nanomaterials by providing high penetration depths, robust transmission data, and simultaneous measurement of multiple Debye–Scherrer rings.[27,28] The micrographs in Fig.1A illustrate that the temperature and time of anneal can drive the characteristic, nanoscale size to grow at various rates. Most importantly, the evolution of this size is clearly reflected by the widths (β) of the XRD peaks (*i.e.*, Figs. 1B-D). Additionally, Fig.1D shows that the magnitude of β can depend on width type. This observation suggests that the choice between F and I impacts the results of width methods.

Atomistic Simulation

To evaluate the accuracies of width methods in experimentally realistic scenarios, we used 3.4-million-atom simulations of a nanocrystalline, Ni nanowire subjected to thermal and mechanical loads in a prior study.[29] Figures 2A-D present cross-sectional microstructures at the initial state, after 40 ns of anneal alone, after 40 ns of anneal + creep, and after 40 ns of anneal + fatigue. Face-centered-cubic (FCC) atoms are colored from blue to red according to the sizes of the coherent domains (*i.e.*, regions without line/planar defects). Single and

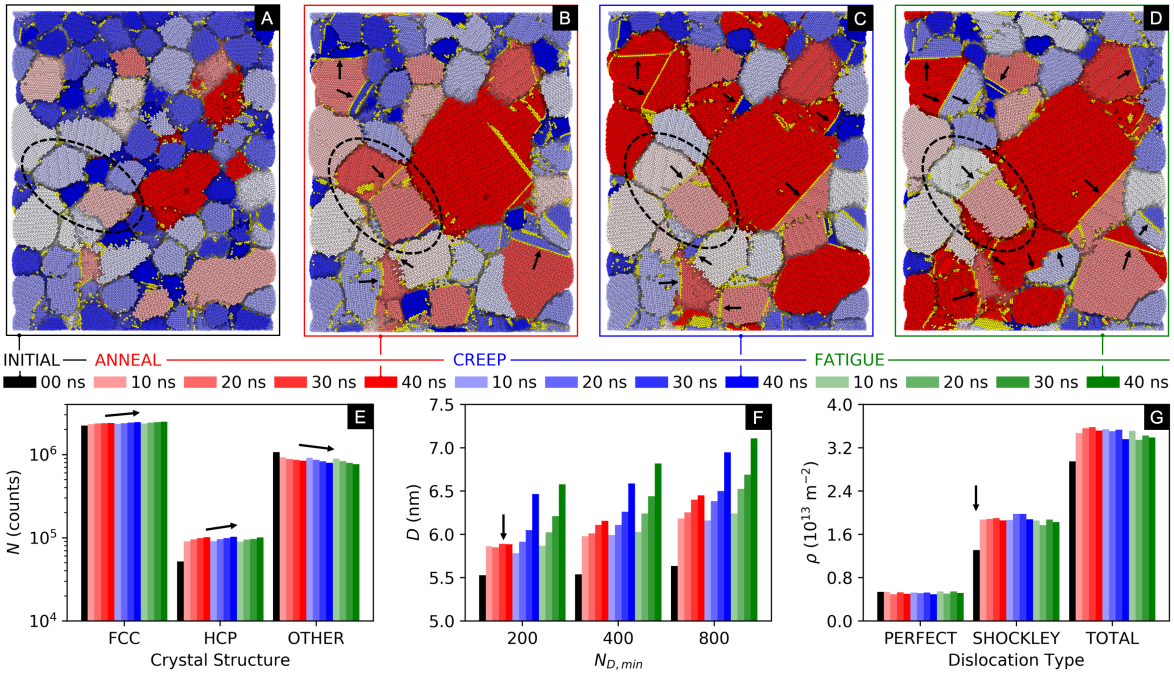

Figure 2. Microstructures for the simulated nanowire at the (A) initial, (B) anneal, (C) creep, and (D) fatigue states. FCC atoms are colored blue to red according to the sizes of the coherent domains. Single and double planes of yellow, HCP atoms represent twins and stacking faults, respectively. Atoms of other coordinations are hidden. Discrete characterizations include (E) number of atoms per crystal structure (N), (F) volume-averaged domain size (D) as a function of the minimum number of atoms per domain ($N_{D,min}$), and (G) dislocation density (ρ).

double planes of yellow hexagonal-close-packed (HCP) atoms represent twins and stacking faults, respectively. Other atoms, which comprise the grain boundaries, are hidden.

Both the thermal and mechanical loads induced grain growth. For example, the largest grain grew significantly after 40 ns of anneal alone (*i.e.*, Fig.2B), more after 40 ns of anneal + creep (*i.e.*, Fig.2C), and even more after 40 ns of anneal + fatigue (*i.e.*, Fig.2D). The increasing number (N) of FCC-coordinated atoms and the decreasing number of other-coordinated atoms (*i.e.*, Fig.2E) indirectly reflects these differences in grain growth. Consistent with prior evidence,[30–32] grain rotation and twinning drove grain growth in all three cases. As illustrated by the numerous black arrows in Figs. 2B-D, all three loads forced domains to rotate/shift to satisfy the twin angle and then merge into twinned grains. This proposed grain-growth mechanism is consistent with the increasing N of HCP-coordinated atoms with respect to time for each load in Fig.2E. By producing different amounts of grain growth and likely activating different mechanisms, these three simulations well established ground truths for validating the width methods.

Figure 2F presents the evolution of the volume-averaged domain size (D) of the nanowire. Coherent domains better served as an evaluation metric for the width methods than poten-

tially twinned grains because diffraction results from coherent interference. As detailed in the Methods Section, D was computed through a clustering algorithm,[33] which required selection of a minimum number of atoms per domain ($N_{D,min}$). Setting $N_{D,min} > 200$ atoms ensured an increasing D, which was reflected by Figs. 2A-E. Overall, this ground truth required width methods to produce D values between roughly 5.5 nm (*i.e.*, at the initial state) and 6.8 nm (*i.e.*, at 40 ns of fatigue) with an initial jump between 0 ns and 10 ns.

Figure 2G presents the evolution of the dislocation density (ρ) of the nanowire. Enhanced dislocation-motion resistance common to nanocrystalline materials[34] likely maintained the constant number of perfect dislocations. The only major change in ρ was the initial jump in Shockley dislocations, which accompany stacking faults. Some faulting must have occurred but was arrested quickly in all three loading cases. This inference is consistent with the rarity of double planes of HCP atoms in the micrographs in Figs. 2A-D. Overall, the second ground truth required the ρ produced from width methods to have an order of magnitude of $10^{13}/m^2$ and be relatively constant after an initial jump between 0 ns and 10 ns of each load.

Virtual Diffraction

We next employed the LAMMPS user-diffraction package[35,36] to simulate conventional XRD of the nanocrystalline nanowire at the initial state and after four, 10-ns increments of anneal, creep, and fatigue. This package had already successfully detailed deformation mechanisms

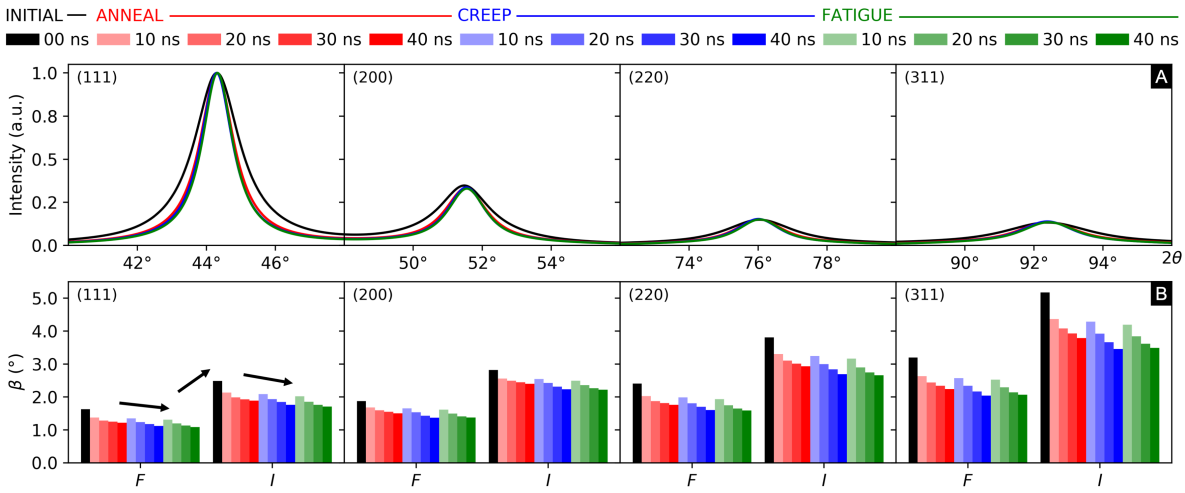

Figure 3. (A) Virtual diffractograms and (B) peak widths (β) for the nanowire at the initial, anneal, creep, and fatigue states. The magnitude of β changed with load, crystallographic plane (hkl), and width type (*i.e.*, F vs. I). For visual convenience, only the 0-ns and 40-ns states are plotted in (A). In (B), all five time steps are plotted for each load.

in nanocrystalline copper.[37] Fig.3A shows pseudo-Voigt curve fits for the first four XRD peaks after 40 ns of each load. Fig.3B shows the the peak widths (β) in terms of both F and I for all 10-ns increments. Despite a difference of twelve orders of magnitude in time scale, both the synchrotron diffraction and the virtual diffraction exemplified measurable connections between peak broadening and the characteristic, nanoscale size (*i.e.*, Figs. 1A and 1C vs. Figs. 2F and 3B). As with our experiments, the magnitude of β depended not only on the crystallographic plane (hkl) but also on the width type (*i.e.*, Fig.1D and Fig.3B).

Width Methods

As mathematically detailed in the Methods Section, width methods can vary by (1) broadening sources (*e.g.*, D, ϵ, σ, u, ρ, and Q), (2) width type (*e.g.*, F and I), and (3) functional forms (*e.g.*, Lorentzians and Gaussians). Therefore, to systematically survey the width methods, we first introduced a consistent nomenclature, which denotes the width type and then the broadening source(s). For example, "F:D" represents the Scherrer Method applied to full-width-half-max data. For multi-term models, the nomenclature also exponentiates the broadening sources according to the functional forms used to convolve the terms (*e.g.*, 1 for a Lorentzian form and 2 for a Gaussian form). For example, "I:$D^1\epsilon^1$" represents the Lorentzian form of the traditional Williamson-Hall Method applied to integral-breadth data. Guided by this consistent nomenclature, we selected the twenty-two width methods listed at the bottom of Fig.4 to mathematically bound the useful solutions.

To evaluate the accuracies of these width methods, Fig.4 presents three evaluation metrics: (1) coefficient of determination for fit to the width method (R^2), (2) volume-averaged domain size of the nanowire (D), and dislocation density of the nanowire (ρ). As common in statistical analysis, we required that $R^2 \geq 0.95$ to ensure that the methods fit the β data well. To match the ground truth of D from the atomistic simulations (*i.e.*, Fig.2H), we required D to increase from ≈ 5.5 nm at the initial state to ≈ 7 nm after 40 ns of anneal. For convenience, Fig.4 highlights these target regions of R^2 and D in grey. Because the coefficient for ρ in the Dislocation Methods is poorly established,[38,39] we only required that the resulting trends and order of magnitude of ρ match those of the ground truth (*i.e.*, an initial jump and then a flatline at $\approx 10^{13}/m^2$).

Despite their simplicity, the Scherrer Methods (*i.e.*, F:D and I:D) produced the highest values of R^2 for the initial microstructure (*i.e.*, Fig.4A). Further, both Scherrer Methods correctly produced an increase in D with respect to loading time (*i.e.*, Figs. 4B). I:D even had the correct magnitudes. These observations support the frequent use of the Scherrer Method to assess unloaded nanomaterials.[2,4,5,8,9] However, thermal and mechanical loads rapidly de-

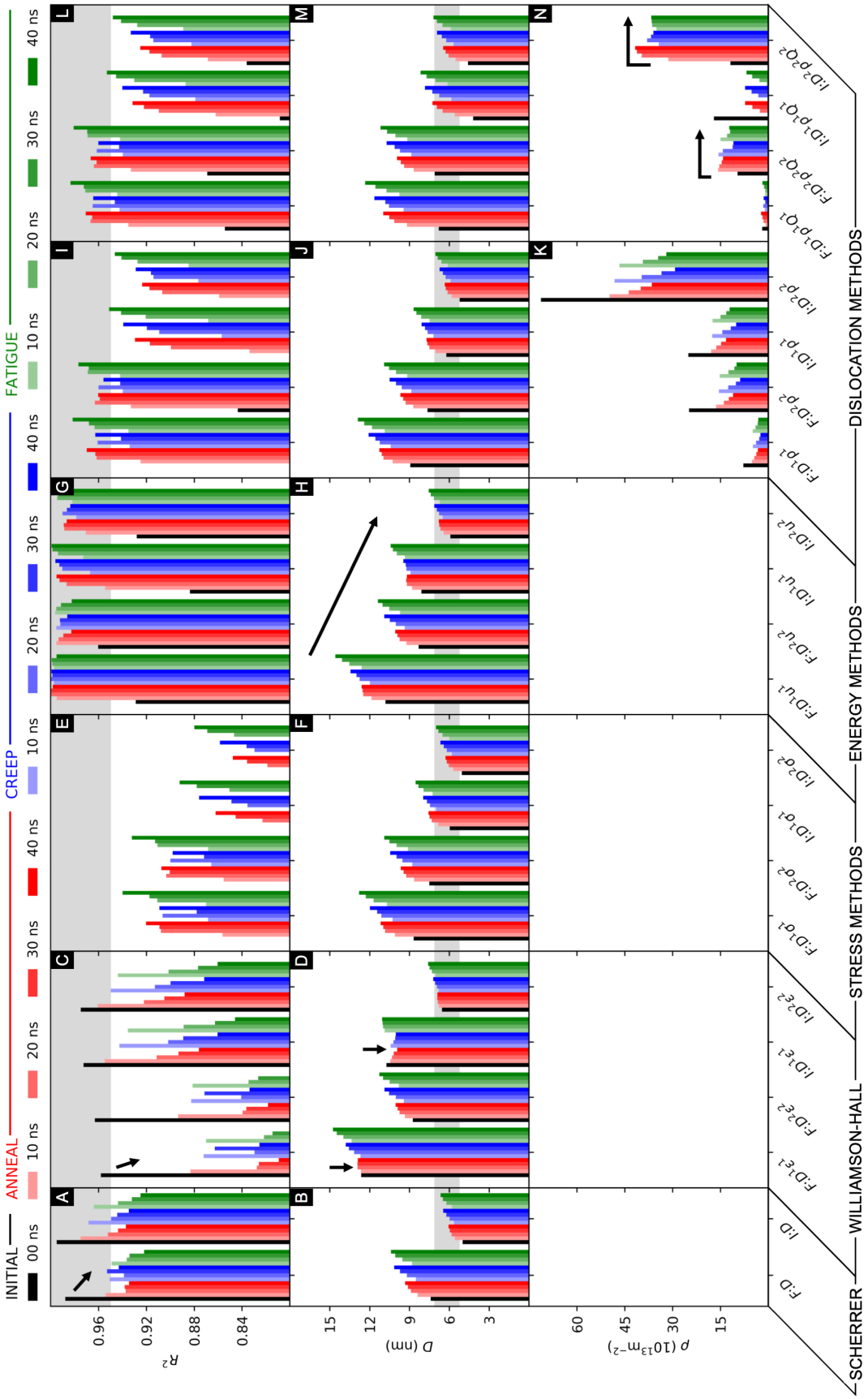

Figure 4. Coefficient of determination for the method fit (R^2), size of the coherently diffracting domains of the nanowire (D), and density of dislocations for the nanowire (ρ) for twenty-two, representative width methods applied to virtual diffractograms from the nanocrystalline nanowire. All three elements of the consistent nomenclature (*i.e.*, broadening sources, width type, and functional forms) quantitatively and qualitatively affected the results. Grey regions indicate consistency with the target regions of R^2 and D.

graded R^2 (*i.e.*, Fig.4A). As the values of D rose, the importance of ϵ broadening likely grew. Overall, the Scherrer Methods seem most useful for assessing unloaded nanomaterials.

To assess loaded nanomaterials, one may have thought to prefer the traditional Williamson-Hall Methods, which include an ϵ term. However, these methods surrendered R^2 with respect to loading time (*i.e.*, Fig.4C) even faster than the Scherrer Methods (*i.e.*, Fig.4A). Whereas fitting to a Scherrer Method typically allows an arbitrary, variable intercept, fitting to the Williamson-Hall Methods problematically forces that intercept to result in a single value of ϵ. Alarmingly, the rapid loss in R^2 even coincided with incorrect trends in D (*i.e.*, Fig. 4D) for the two most popular methods. $F\text{:}D^1\epsilon^1$ incorrectly showed no difference in D between 0 ns and 10 ns of anneal, and $I\text{:}D^1\epsilon^1$ non-physically produced a decreasing trend in D for both anneal and creep. The fact that the two most popular width methods predicted incorrect trends strongly demonstrates the importance of rationally selecting a width method.

In contrast to the traditional Williamson-Hall Methods, the Stress Methods and Energy Methods introduced microstrain anisotropy by substituting ϵ for σ or u through linear elasticity. Correspondingly, all Stress Methods and Energy Methods correctly produced an upward trend in D (*i.e.*, Figs. 4F,H). Interestingly, these methods and others cleanly illustrated that both the width type and the functional forms can systematically scale D in the following order: F + Lorentzian forms, F + Gaussians forms, I + Lorentzian forms, and I + Gaussian forms (*e.g.*, black arrow in Fig.4H). The methods with Gaussian forms and I best matched the ground-truth values of D. However, while the Stress Methods and the Energy Methods produced similar trends and magnitudes of D, the latter had significantly higher values of R^2 (*i.e.*, Figs. 4E,G). In fact, the Energy Methods outperformed all others in terms of R^2 for characterizing the loaded nanowire. This takeaway is interesting in light of the rarity of the appearance of Energy Methods, which only require the commonly available the Young's Modulus (E) in terms of material properties.

By including anisotropy through dislocation-contrast factors (C), the Dislocation Methods also outperformed the Scherrer Methods and the traditional Williamson-Hall Methods in characterizing the loaded nanowire (*i.e.*, Figs. 4I,L). All Dislocation Methods correctly produced an upward trend in D (*i.e.*, Figs. 4J,M) and a $10^{13}/\text{m}^2$ order of magnitude for ρ (*i.e.*, Figs. 4K,N). Interestingly, including the high-order Q broadening marginally affected R^2 and D but strongly affected the trends in ρ. In particular, only the width methods that represented broadening from D, ρ, and Q with Gaussian forms (*i.e.*, $F\text{:}D^2\rho^2Q^2$ and $I\text{:}D^2\rho^2Q^2$) correctly reproduced an initial jump and then flatline in ρ. Therefore, for quantifying dislocation density, we caution against using the "Simplified Modified Williamson-Hall Methods," which include ρ broadening but not Q broadening.[40] Considering both the predicted values of D and the trends in ρ, we consider $I\text{:}D^2\rho^2Q^2$ the best Dislocation Methods.

In addition to accuracies, we should consider the conveniences of width methods. The Scherrer Methods and the traditional Williamson-Hall Methods are the most popular methods today because they require no material-specific information. If the goal is to characterize D in an unloaded nanomaterial, we recommend the Scherrer Methods (*e.g.*, I:D). If the goal is to characterize ϵ, and no material properties are available, it is important to recognize the high potential for systematic error when applying the traditional Williamson-Hall Methods (*e.g.*, Fig.4D), which non-physically force a single value of ϵ. Alternatively, if material properties are available, the Energy Methods and the Dislocation Methods offer improved characterizations for thermally/mechanically loaded nanomaterials. If the goal is to characterize D, ϵ, σ, or u, we recommend the rare yet simple Energy Methods (*e.g.*, I:D^2u^2), which only require the readily available elastic constants in terms of material-specific properties. The Dislocation Methods can also predict D well for loaded nanomaterials. However, the researcher must carefully consider the effects of not only the width type, broadening sources, and functional forms (*e.g.*, Figs. 4K,N) but also the dislocation-contrast factors (C). These factors vary with the material, crystallographic plane, and the assumed ratio of dislocation types. If the goal is to characterize ρ, the Dislocation Methods are the only options within width methods. Alternatively, researchers may consider more complicated approaches, such as Variance Methods,[41] Modified Warren-Averbach Methods,[19,42] Reitveld Refinement,[43] and Whole Powder Pattern Modeling.[44]

Conclusions

We evaluated the accuracies and conveniences of twenty-two width methods by assessing X-ray diffractograms generated from atomistic simulations of a nanocrystalline, Ni nanowire subjected to anneal, creep, and fatigue. These experimentally consistent simulations provided reliable ground truths for the direct evaluation of width methods. Major takeaways include:

1. The results of width methods can vary both quantitatively and qualitatively when altering the broadening sources (*e.g.*, domain size, microstrain, deformation energy, dislocation density, and dislocation correlation), width type (*e.g.*, full-width-half-max vs. integral breadth), or functional forms (*e.g.*, Lorentzian vs. Gaussian). This finding emphasizes the advantage of our consistent nomenclature over the traditional ones, which can overlap and mislead.

2. The Scherrer Methods, which attribute peak broadening exclusively to domain size, predictably characterized the initial microstructure well but rapidly lost accuracy when

thermal or mechanical loads induced microstrain. Hence, we recommend the Scherrer Methods for analyzing unloaded nanomaterials only.

3. Surprisingly, the Williamson-Hall Methods, which are the most prevalent methods today, performed even worse than the Scherrer Methods by forcing a single value of microstrain. In fact, some of these methods even resulted in trends that opposed those of the ground truths of the atomistic simulations (*e.g.,* a decrease in domain size with annealing time). Overall, we recommend against using the Williamson-Hall Methods despite their conveniences.

4. The rarely employed Energy Methods well characterized the thermally and mechanically loaded states despite conveniently only requiring the elastic constants in terms of material properties. Out of all tested width methods, we recommend $I{:}D^2u^2$ for assessing the characteristic size, strain, stress, or deformation energy of loaded nanomaterials.

5. When including higher-order terms (*e.g.*, $I{:}D^2\rho^2Q^2$), the anisotropic Dislocation Methods well quantified the characteristic size and the dislocation density. However, these methods require multiple material-specific factors and poorly established coefficients. If dislocation information is desired, we recommend the Dislocation Methods if the numerous variables are carefully considered.

Overall, our work improved the utility of XRD in experimentally characterizing a variety of nanomaterials. We assessed nanocrystalline Ni, which is frequently considered a representative metallic system because of the ease of manufacturing and the prevalence of FCC metals in structural applications. While other metallic systems likely follow trends similar to those shown in the current work, a systematic sensitivity analysis is beyond the scope of the present work. Although the precise details may change from system to system, we generally expect that all materials will be subjected to biases, such as those revealed by the present study. Further, our finding that all three elements of the consistent nomenclature can influence the resulting properties applies to an even broader range of nanomaterials (*e.g.*, both metals and ceramics). To select an appropriate width method, a researcher would simply employ our consistent nomenclature to systematically survey the numerous width methods for the nanomaterial of interest. This process would be increasingly important when introducing complexity in the material composition, microstructure, and/or loading.

Methods

Synchrotron Diffraction

Experimentation followed previously reported procedures for both processing and characterization.[45] An electrodeposition via the direct-LIGA process (*i.e.*, Lithography, Electroplating, and Molding) produced nanocrystalline alloys with 78 wt% Ni and 22 wt% Fe. Annealing the samples at 470 K (*i.e.*, for 10, 100, and 1000 minutes), 670 K (*i.e.*, for 1, 10, and 100 minutes), and 870 K (*i.e.*, at 1, 10, and 100 minutes) evolved the grain sizes. We characterize the alloys by using scanning electron microscopy and transmission X-ray diffraction (*i.e.*, $E = 12.7$ keV and $\lambda = 0.976$ Å, Stanford Synchrotron Radiation Lightsource (SSRL) beamline 11-3).

Atomistic Simulation

The atomistic model of the nanocrystalline, Ni nanowire was previously constructed[29] by (1) filling a cylindrical volume with solid spheres, (2) evolving those spheres into a microstructure through a recently developed phase-field method,[46] (3) populating each grain within this synthetic microstructure with randomly oriented atomic lattices, and (4) annealing the microstructure. This nanowire had a 35-nm diameter, a 41-nm length, 3.4 million atoms, and approximately 500 domains with an average equivalent spherical diameter around 6 nm. Unlike the traditional Voronoi method, this phase-field method for constructing a nanocrystalline microstructure produced curved grain boundaries and realistic triple junctions.

The nanowire was evolved through simulations of anneal, creep and fatigue through the Large-scale Atomic/Molecular Massively Parallel Simulator (LAMMPS).[29,47] To accurately model the twinning-dominated, grain-size evolution, an embedded-atom-method potential (EAM) for Ni was chosen for emphasis on reproducing experimental stacking-fault energy.[48] All three loads were simulated at a temperature of 500 K for 40 million 1-fs time steps, which translated to a total of 40 ns of simulation time. Periodic boundary conditions along the length of the nanowire approximated an infinitely long nanowire. To echo a stress-relaxation experiment, creep was simulated by applying a uniform displacement of 1% along the length of the nanowire for 0.1 ns and then holding that strain for the remainder of the 40 ns. Fatigue was simulated by applying 200, 0.2-ns cycles (*i.e.*, loading frequency of 5 GHz and strain rate of $10^8/s$) of pulsating tension (*i.e.*, $R = 0$) with a maximum strain of 1%.

For discrete quantification of the atomistic simulations, we used a custom version of Ovito 2.6.1[33] for "Grain Segmentation" and a developer version of Ovito 3.0.0[49] for "Common Neighbor Analysis," "Dislocation Analysis," and "Construct Surface Mesh." The Grain-

Segmentation module, which was created to identify twinning,[33] actually identified coherent domains. To compute the domain size (D), the Grain-Segmentation algorithm first grouped the atoms into coherent domains and assigned grain-boundary atoms to nearby domains by forcing a minimum number of atoms per domain ($N_{D,min}$). Then, the average number of atoms per domain was converted into an equivalent, spherical diameter (*i.e.*, D) by using the atomic density of a Ni unit cell. Dislocation densities were computed by dividing dislocation lengths, which were computed by "Dislocation Analysis," by solid volume, which was computed from "Construct Surface Mesh."

Virtual Diffraction

We simulated conventional XRD of the nanocrystalline nanowire at the initial state and after four, 10-ns increments of the anneal, creep, and fatigue through the LAMMPS user-diffraction module.[35,36] This module kinematically computed XRD intensity for a range of diffraction angles (θ):

$$\text{Intensity} = \left(\frac{1+\cos^2(2\theta)}{\cos(\theta)\sin^2(\theta)}\right)\left(\frac{F(\mathbf{K})F^*(\mathbf{K})}{N}\right), \tag{1}$$

where the first factor covers Lorentz polarization; N is the number of atoms; and F is the structure factor (with conjugate F^*), which is given by:

$$F = \sum_{j=1}^{N} f_j \exp\left(2\pi i \mathbf{K}\cdot\mathbf{r_j}\right), \tag{2}$$

where f is the atomic-scattering factor; $\mathbf{r}$ is the atomic position; and $\mathbf{K}$ is the diffraction vector, which is the difference between the diffraction vector ($\mathbf{K_D}$) and the incident vector ($\mathbf{K_I}$). Bragg's law governs the magnitude of $\mathbf{K}$:

$$|\mathbf{K_D}-\mathbf{K_I}| = |\mathbf{K}| = K = \frac{1}{d} = \frac{2\sin(\theta_c)}{\lambda}, \tag{3}$$

where d is the characteristic diffraction length (*e.g.*, planar spacing for crystals); θ_c is the diffraction angle satisfying Bragg's law; and λ is the X-ray wavelength. In the current study, we used conventional Cu Kα radiation (*i.e.*, $\lambda = 1.54$ Å, $E \approx 8.04$ keV).

Width Methods

The diffractogram of a perfect, infinite crystal would comprise Dirac delta functions at the peak locations that exactly satisfy Bragg's law (*i.e.*, at $2\theta_c$). However, defects (*e.g.*,

sample surfaces, grain boundaries, twin boundaries, and dislocations) broaden the peaks. Differentiating Eq. 3 with respect to θ_c yields total broadening (∂K) as a function of peak width (*i.e.*, $\beta = \partial 2\theta_c$):

$$\partial K = \frac{2\cos(\theta_c)\partial\theta_c}{\lambda} = \frac{\beta\cos(\theta_c)}{\lambda}. \quad (4)$$

Eq. 4 is at the heart of all width methods, which essentially translate β-θ_c data into various representations of ∂K to yield crystallographic information. Therefore, to apply width methods, we first fit the virtual diffractograms with pseudo-Voigt curves, which approximate the convolution of Lorentzian curves with Gaussian curves.[50] From these fits, we computed the values of θ_c and the two most common forms of β: full-width-half-max width (F) (*i.e.*, peak width at half amplitude) and integral-breadth width (I) (*i.e.*, peak area divided by peak amplitude). As for interpreting ∂K, the remaining subsections cover the constituent broadening sources and the common methods for combining them.

Domain-Size Broadening

Especially for nanomaterials, broadening due to the domain boundaries (*i.e.*, ∂K_D) dominates all other broadening sources:

$$\partial K_D = \frac{A_D}{L} = \frac{4A_D}{3D}, \quad (5)$$

where L and A_D represent a characteristic length and shape, respectively.[10,22]

Although Scherrer originally correlated β with crystallite size (D),[10] the characteristic length produced by width methods is actually the length of the coherently diffracting column of material (L).[7] For polycrystalline materials, this column cuts through multiple grains, which comprise crystallites, which comprise domains. Assuming no two domains in the irradiated column interfere coherently, L equals the diameter of a coherently diffracting, spherical domain when the column exactly bisects the domain. Hence, the volume-averaged diameter of a spherical domain (D) approximately equals $4L/3$. Unfortunately, modern studies[25,26] often neglected to convert L to D, so the volume-averaged sizes predicted from width methods arbitrarily seemed closer to the area-averaged sizes from electron microscopy.

This manuscript uses "A_D" for the shape factor rather than the typical "K" to avoid confusion with the magnitude of the diffraction vector (*i.e.*, K in Eq. 3). This coefficient accounts for the effect of domain shapes on ∂K_D.[21] For a uniform distribution of spherical domains, $A_D \approx 0.829$ for F data and 1.704 for I data. For a uniform distribution of non-spherical domains, A_D also changes with crystallographic plane. For a uniform distribution of octahedral domains, $A_D \approx 0.874$ for F data and 1.077 for I data when assessing the first four

XRD peaks of an FCC material. Non-uniform distributions, such as the log-normal function typically used to model grain-size distribution, reduce A_D. Because of these complexities, most studies assume a value of 0.9, 0.94, or 1.0.[2,51,52] We used $A_D = 0.9$, the most common value. Researchers may adjust A_D to scale the resulting values of D but not to remedy incorrect trends.

Microstrain Broadening

Microstrain broadening (∂K_ϵ), which increases with D, can be represented as a function of K (*i.e.*, Eq. 3) and a root-mean-square (RMS) ϵ.[14,15] Alternatively, linear elasticity can substitute ϵ for stress (σ) or deformation energy (u):[16]

$$(\partial K_\epsilon, \partial K_\sigma, \partial K_u) = \left(2K\epsilon, 2K\frac{\sigma}{E}, 2K\sqrt{\frac{2u}{E}}\right), \tag{6}$$

where Young's modulus (E) varies with crystallographic plane (hkl) and the elastic constants (C_{ij}). For a cubic crystal[53],

$$\begin{aligned} E^{-1} &= S_{11} - 2\left(S_{11} + 2S_{12} - S_{44}\right)\left(\frac{h^2k^2 + h^2l^2 + k^2l^2}{\left(h^2 + k^2 + l^2\right)^2}\right), \\ S_{11} &= (C_{11} + C_{12})(C_{11} - C_{12})^{-1}(C_{11} + 2C_{12})^{-1}, \\ S_{12} &= (-C_{12})(C_{11} - C_{12})^{-1}(C_{11} + 2C_{12})^{-1}, \\ S_{44} &= (C_{44})^{-1}. \end{aligned} \tag{7}$$

For Ni, (C_{11}, C_{12}, C_{44}) = (243.6, 149.4, 119.6) GPa,[18] so ($E_{111}, E_{200}, E_{220}, E_{311}$) = (294, 130, 224, 176) GPa. For evaluating the accuracies of the width methods, we avoided ϵ as a ground truth because much debate surrounds the form and origin of ϵ.[54–56] Most argue that ϵ represents an RMS value instead of a maximum value, but no clear consensus exists on the extent of the influence of the boundaries on ϵ.

Dislocation Broadening

Anisotropic microstrain can also be modeled through dislocation density (ρ) and dislocation correlation (Q):[19,20]

$$\partial K_\rho = A_\rho\sqrt{\rho\left(\frac{\pi K^2 b^2 C}{2}\right)^1} = \left(\frac{\sqrt{2\pi}A_\rho b}{\lambda}\sqrt{\rho}\right)\sqrt{C}\sin(\theta), \tag{8}$$

$$\partial K_Q = A_Q \sqrt{Q \left(\frac{\pi K^2 b^2 C}{2} \right)^2} = \left(\frac{2\pi A_Q b^2}{\lambda^2} \sqrt{Q} \right) C \sin^2(\theta), \tag{9}$$

where b, A_ρ, A_Q, and C are the Burger's-vector magnitude, dislocation coefficient, dislocation-correlation coefficient, and the dislocation-contrast factor. A_ρ depends on the effective outer cutoff radius of dislocations but is not well established. We employed $A_\rho = 10$, which was mathematically supported for a wide range of dislocation densities[17] and employed in the original study on Fe.[38] However, a recent experimental study on the X-ray/neutron diffraction of aluminum suggested $A_\rho \approx 0.6$.[39] Because A_Q is even less established than A_ρ, values of Q are not typically interpreted. As in other works,[39] we used the b corresponding to perfect dislocations (*i.e.*, $a/\sqrt{2} \approx 0.249$ nm for Ni). Most importantly, the dislocation contrast factor (C) captures anisotropy by relating the line vector ($\mathbf{l}$), Burgers vector ($\mathbf{b}$), and diffraction vector ($\mathbf{K}$).[18] Untextured samples or randomly oriented Burgers vectors enable the use of average contrast factors ($\overline{C}$). For a cubic crystal,

$$C \approx \overline{C} = \overline{C}_{h00} \left(1 - q \left(\frac{h^2k^2 + h^2l^2 + k^2l^2}{\left(h^2 + k^2 + l^2\right)^2} \right) \right), \tag{10}$$

where $\overline{C}_{h00}$ and q can be expressed as exponential functions of C_{ij} through tables in a prior publication.[18] We assumed a 50-50 distribution of edge and screw dislocations in Ni to obtain $\overline{C}_{h00} \approx 0.266$ and $q \approx 2.35$. Alternatively, the values of C_{hoo} and q can be deduced from experimental fits.[57]

Planar-Defect Broadening

Especially for nanocrystalline materials, planar defects (P) may divide grains into multiple, coherently diffracting domains. To adjust the predicted size closer to the grain size, some Dislocation Methods included a P term as well:[20]

$$\partial K_P = p\omega = \left(\frac{1.5\rho_f + \rho_\tau}{a} \right) \sum_B \left(\frac{|h + k + l|}{(U + B)\sqrt{h^2 + k^2 + l^2}} \right), \tag{11}$$

where ρ_f is the density of stacking faults; ρ_τ is the density of twins; a is the lattice parameter; U is the number of unbroadened peaks; and B is the number of broadened peaks.

Combined Broadening

Because nanomaterials have many boundaries, studies often employ the Scherrer Method,[10,22] which attributes all broadening to D. Equating Eqs. 4 and 5 yields:

$$\beta\cos(\theta) = \frac{4A_D\lambda}{3D}. \tag{12}$$

Typically, researchers allow a non-zero intercept when fitting to Eq. 12. Equivalently, we fit to the Modified Scherrer Method,[12] which applies a logarithmic transform to Eq. 12:

$$\ln\beta = \left(\ln\frac{4A_D\lambda}{3D}\right) + \ln\frac{1}{\cos(\theta)}. \tag{13}$$

Because the Scherrer Method has one independent variable (*i.e.*, D), only one XRD peak is needed. Assessing multiple peaks improves the accuracy and can indicate the presence of anisotropic ϵ. Alternatively, ϵ can be modeled directly by convolving a term relating to size with term(s) relating to strain:[52]

$$1 = \sum_i \left(\frac{\partial K_i}{\partial K}\right)^{a_i}, \tag{14}$$

where i denotes the broadening sources, which may include domain boundaries (D), planar defects (P), microstrain (ϵ), stress (σ), deformation energy (u), dislocation density (ρ), and dislocation correlation (Q). To avoid redundancy, only one broadening source related to strain (*i.e.*, ϵ, σ, u, or ρ) can be selected. Choosing ρ enables the additional option of the higher-order term related to Q. Because each of these broadening sources introduces one independent variable, the total number of broadening terms must not exceed the number of XRD peaks analyzed. As in the consistent nomenclature, the superscripts (a_i) dictate the functional forms (*e.g.*, $a_i = 1$ for Lorentzian, and $a_i = 2$ or Gaussian).

The most popular Williamson-Hall Method[14] incorporates a Lorentzian D term and a Lorentzian ϵ term. Substituting Eqs. 4, 5 and 6 into Eq. 14 with $a_D = a_\epsilon = 1$ yields:

$$\beta\cos\theta = \left(\frac{4A_D\lambda}{3D}\right) + (4\epsilon)\sin(\theta), \tag{15}$$

where D and ϵ can be determined from the intercept and slope, respectively. From this single value of ϵ, RMS values of σ and u can be computed through linear elasticity. Because only a single value of ϵ is calculated, Eq. 15 is misleadingly called the "Williamson-Hall Uniform Deformation Model." Because a uniform deformation would shift not broaden the peaks,[52] we prefer the consistent nomenclature (*i.e.*, $D^1\epsilon^1$).

To introduce microstrain anisotropy, the Williamson-Hall Uniform-Stress-Deformation Model[16] uses E to exchange ∂K_ϵ for ∂K_σ (*i.e.*, Eq. 6). For Lorentzian functional forms (*i.e.*, $D^1\sigma^1$),

$$\beta\cos\theta = \left(\frac{4A_D\lambda}{3D}\right) + (4\sigma)\,\frac{\sin(\theta)}{E}. \tag{16}$$

Likewise, the Williamson-Hall Uniform-Deformation-Energy-Density Model[16] uses E to exchange ∂K_ϵ for ∂K_u. For Lorentzian functional forms (*i.e.*, D^1u^1),

$$\beta\cos\theta = \left(\frac{4A_D\lambda}{3D}\right) + \left(\sqrt{32}\sqrt{u}\right)\frac{\sin(\theta)}{\sqrt{E}}. \tag{17}$$

Alternatively, the Dislocation Methods introduce anisotropy by using C. These methods incorporate ∂K_ρ and potentially also ∂K_Q and/or ∂K_P.[19,20] To represent the most general Dislocation Method with Lorentzian forms (*i.e.*, $D^1\rho^1Q^1P^1$), we substituted Eqs. 5, 8, 9, and 11 into Eq. 14 with $a_i = 1$:

$$\beta\cos(\theta) = \left(\frac{4A_D\lambda}{3D}\right) + (p\lambda)\,\omega + \left(\sqrt{2\pi}A_\rho b\sqrt{\rho}\right)\sqrt{C}\sin(\theta) + \left(\frac{2\pi A_Q b^2}{\lambda}\sqrt{Q}\right)C\sin^2(\theta), \tag{18}$$

The first two broadening terms relate to size effects, and the last two terms relate to strain effects. Because each additional broadening source requires additional coefficients and an extra XRD peak, common width methods omit terms from Eq. 18. For example, we evaluated the importance of the second-order Q term by testing models with and without it (*e.g.*, $I{:}D^1\rho^1$ vs. $I{:}D^1\rho^1Q^1$). To ensure a 1:1 comparison between the discrete D and the sizes predicted by width methods, we did not examine methods with ∂K_P.

Eq. 14 and our consistent nomenclature accommodate many types and combinations of functional forms. For survey purposes, we tested models that exclusively employ Lorentzian forms (*i.e.*, all $a_i = 1$) or Gaussian forms (*i.e.*, all $a_i = 2$). Because all broadening sources comprise only one term, pure-Gaussian models derived as termwise squares of the pure-Lorentzian models detailed above. Mixed-form methods, such as the Halder-Wagner Methods[23,58] (*e.g.*, $F{:}D^1\epsilon^2$) and the asymmetric variants of the Modified Williamson-Hall Methods (*e.g.*, $I{:}D^1\rho^2Q^2$),[24] would produce results between those of the tested extremes.

Acknowledgments

The authors thank D. Medlin from Sandia National Laboratories (SNL) for technical commentary, A. Stukowski from the Darmstadt University of Technology for a developer version of OVITO, and J. Weeks from Word Tree Consulting for editing. This work was supported

by the United States (US) Department of Energy (DOE) Office of Basic Energy Sciences (BES), Department of Materials Science and Engineering. Experimental X-ray diffraction was performed at the Stanford Synchrotron Radiation Lightsource (SSRL), an Office of Science user facility operated for the US DOE. Virtual-diffraction capabilities were provided by the Center for Integrated Nanotechnologies (CINT), an Office of Science user facility operated for the US DOE by SNL, a multi-mission laboratory managed and operated by National Technology and Engineering Solutions of Sandia (NTESS), LLC, a wholly owned subsidiary of Honeywell International, Inc., for the US DOE's National Nuclear Security Administration (NNSA) under contract DE-NA0003525. The views expressed in this article do not necessarily represent the views of the US DOE or the US Government.

References

(1) Weidenthaler, C. Pitfalls in the characterization of nanoporous and nanosized materials. *Nanoscale* **2011**, *3*, 792–810.

(2) Holder, C.; Schaak, R. Tutorial on Powder X-ray Diffraction for Characterizing Nanoscale Materials. *ACS Nano* **2019**, *13*, 7359–7365.

(3) Li, T.; Senesi, A.; Lee, B. Small angle X-ray scattering for nanoparticle research. *Chemical Reviews* **2016**, *116*, 11128–11180.

(4) Yu, T.; Shen, Z.; Toh, W.; Xue, J.; Wang, J. Size effect on the ferroelectric phase transition in $SrBi_2Ta_2O_9$ nanoparticles. *Journal of Applied Physics* **2003**, *94*, 618–620.

(5) Niekiel, F.; Bitzek, E.; Spiecker, E. Combining atomistic simulation and X-ray diffraction for the characterization of nanostructures: A case study on fivefold twinned nanowires. *ACS Nano* **2014**, *8*, 1629–1638.

(6) Al-Ghamdi, A.; Al-Hazmi, F.; Alnowaiser, F.; Al-Tuwirqi, R.; Al-Ghamdi, A.; Alhartomy, O.; El-Tantawy, F.; Yakuphanoglu, F. A new facile synthesis of ultra fine magnesium oxide nanowires and optical properties. *Journal of Electroceramics* **2012**, *29*, 198–203.

(7) Kril, C.; Birringer, R. Estimating grain-size distributions in nanocrystalline materials from X-ray diffraction profile analysis. *Philosophical Magazine A* **1998**, *77*, 621–640.

(8) Lefebvre, L.; Chevalier, J.; Gremillard, L.; Zenati, R.; Thollet, G.; Bernache-Assolant, D.; Govin, A. Structural transformations of bioactive glass 45S5 with thermal treatments. *Acta Materialia* **2007**, *55*, 3305–3313.

(9) Lian, J.; Jang, D.; Valdevit, L.; Schaedler, T.; Jacobsen, A.; Carter, W.; Greer, J. Catastrophic vs gradual collapse of thin-walled nanocrystalline Ni hollow cylinders as building blocks of microlattice structures. *Nano Letters* **2011**, *11*, 4118–4125.

(10) Scherrer, P. Determination of the size and internal structure of colloidal particles using X-rays. *Mathematical Physics* **1918**, *2*, 98–100.

(11) Holzwarth, U.; Gibson, N. The Scherrer equation versus the 'Debye-Scherrer equation'. *Nature Nanotechnology* **2011**, *6*, 534.

(12) Monshi, A.; Foroughi, M.; Monshi, M. Modified Scherrer equation to estimate more accurately nano-crystallite size using XRD. *World Journal of Nano Science and Engineering* **2012**, *2*, 154–160.

(13) Scardi, P.; Leoni, M.; Delhez, R. Line broadening analysis using integral breadth methods: A critical review. *Journal of Applied Crystallography* **2004**, *37*, 381–390.

(14) Williamson, G.; Hall, W. X-ray line broadening from filed aluminium and wolfram. *Acta Metallurgica* **1953**, *1*, 22–31.

(15) Stokes, A.; Wilson, A. The diffraction of X rays by distorted crystal aggregates-I. *Proceedings of the Physical Society* **1944**, *56*, 174.

(16) Mote, V.; Purushotham, Y.; Dole, B. Williamson-Hall analysis in estimation of lattice strain in nanometer-sized ZnO particles. *Journal of Theoretical and Applied Physics* **2012**, *6*, 6.

(17) Wilkens, M. The determination of density and distribution of dislocations in deformed single crystals from broadened X-ray diffraction profiles. *Physica Status Solidi (A)* **1970**, *2*, 359–370.

(18) Ungár, T.; Dragomir, I.; Révész, A.; Borbély, A. The contrast factors of dislocations in cubic crystals: the dislocation model of strain anisotropy in practice. *Journal of Applied Crystallography* **1999**, *32*, 992–1002.

(19) Ungár, T.; Borbély, A. The effect of dislocation contrast on X-ray line broadening: A new approach to line profile analysis. *Applied Physics Letters* **1996**, *69*, 3173–3175.

(20) Ungár, T.; Révész, A.; Borbély, A. Dislocations and grain size in electrodeposited nanocrystalline Ni determined by the modified Williamson–Hall and Warren–Averbach procedures. *Journal of Applied Crystallography* **1998**, *31*, 554–558.

(21) Langford, J.; Wilson, A. Scherrer after sixty years: A survey and some new results in the determination of crystallite size. *Journal of Applied Crystallography* **1978**, *11*, 102–113.

(22) Laue, M. Lorentz-Faktor und Intensitätsverteilung in Debye-Scherrer-Ringen. *Zeitschrift für Kristallographie-Crystalline Materials* **1926**, *64*, 115–142.

(23) Halder, N.; Wagner, C. Separation of particle size and lattice strain in integral breadth measurements. *Acta Crystallographica* **1966**, *20*, 312–313.

(24) Bahramyan, M.; Nedjad, S. X-ray diffraction line broadening analysis of nanostructured nickel powder. *Physics of Metals and Metallography* **2017**, *118*, 839–845.

(25) Zak, K.; Majid, W.; Abrishami, E.; Yousefi, R. X-ray analysis of ZnO nanoparticles by Williamson–Hall and size–strain plot methods. *Solid State Sciences* **2011**, *13*, 251–256.

(26) Sivakami, R.; Dhanuskodi, S.; Karvembu, R. Estimation of lattice strain in nanocrystalline RuO_2 by Williamson–Hall and size–strain plot methods. *Spectrochimica Acta Part A: Molecular and Biomolecular Spectroscopy* **2016**, *152*, 43–50.

(27) Lohmiller, J.; Grewer, M.; Braun, C.; Kobler, A.; Kübel, C.; Schüler, K.; Honkimäki, V.; Hahn, H.; Kraft, O.; Birringer, R.; Gruber, P. Untangling dislocation and grain boundary mediated plasticity in nanocrystalline nickel. *Acta Materialia* **2014**, *65*, 295–307.

(28) Holt, M.; Harder, R.; Winarski, R.; Rose, V. Nanoscale hard X-ray microscopy methods for materials studies. *Annual Review of Materials Research* **2013**, *43*, 183–211.

(29) Foiles, S.; Abdeljawad, F.; Moore, A.; Boyce, B. Fatigue-driven acceleration of abnormal grain growth in nanocrystalline wires. *Modelling and Simulation in Materials Science and Engineering* **2019**, *27*, 025008.

(30) Spearot, D.; Tucker, G.; Gupta, A.; Thompson, G. Mechanical properties of stabilized nanocrystalline FCC metals. *Journal of Applied Physics* **2019**, *126*, 110901.

(31) Brons, J.; Hardwick, J.; Padilla II, H.; Hattar, K.; Thompson, G.; Boyce, B. The role of copper twin boundaries in cryogenic indentation-induced grain growth. *Materials Science and Engineering: A* **2014**, *592*, 182–188.

(32) Mahajan, S.; Pande, C.; Imam, M.; Rath, B. Formation of annealing twins in fcc crystals. *Acta Materialia* **1997**, *45*, 2633–2638.

(33) Zepeda-Ruiz, L.; Stukowski, A.; Oppelstrup, T.; Bulatov, V. Probing the limits of metal plasticity with molecular dynamics simulations. *Nature* **2017**, *550*, 492.

(34) Pande, C.; Cooper, K. Nanomechanics of Hall–Petch relationship in nanocrystalline materials. *Progress in Materials Science* **2009**, *54*, 689–706.

(35) Coleman, S.; Spearot, D.; Capolungo, L. Virtual diffraction analysis of Ni [0 1 0] symmetric tilt grain boundaries. *Modelling and Simulation in Materials Science and Engineering* **2013**, *21*, 055020.

(36) Coleman, S.; Sichani, M.; Spearot, D. A computational algorithm to produce virtual X-ray and electron diffraction patterns from atomistic simulations. *JOM* **2014**, *66*, 408–416.

(37) Foley, D.; Coleman, S.; Tschopp, M.; Tucker, G. Correlating deformation mechanisms with X-ray diffraction phenomena in nanocrystalline metals using atomistic simulations. *Computational Materials Science* **2018**, *154*, 178–186.

(38) Révész, A.; Ungár, T.; Borbély, A.; Lendvai, J. Dislocations and grain size in ball-milled iron powder. *Nanostructured Materials* **1996**, *7*, 779–788.

(39) Woo, W.; Ungár, T.; Feng, Z.; Kenik, E.; Clausen, B. X-ray and neutron diffraction measurements of dislocation density and subgrain size in a friction-stir-welded aluminum alloy. *Metallurgical and Materials Transactions A* **2010**, *41*, 1210–1216.

(40) Takaki, S.; Masumura, T.; Tsuchiyama, T. Dislocation characterization by the direct-fitting/modified Williamson–Hall (DF/mWH) method in cold worked ferritic steel. *ISIJ International* **2019**, *59*, 567–572.

(41) Kumar, N.; Krishna, M.; Chandra, S.; Tewari, R. Influence of dislocations and grain boundaries on diffraction line profiles of nano-crystalline materials: A numerical study. *Computational Materials Science* **2020**, *171*, 109213.

(42) Warren, B.; Averbach, B. The separation of cold-work distortion and particle size broadening in X-ray patterns. *Journal of Applied Physics* **1952**, *23*, 497–497.

(43) Young, R. *The Rietveld Method*; 1993; Vol. 5.

(44) Scardi, P.; Ortolani, M.; Leoni, M. WPPM: microstructural analysis beyond the Rietveld method. Materials Science Forum. 2010; pp 155–171.

(45) Boyce, B.; Furnish, T.; Padilla, H.; Campen, D.; Mehta, A. Detecting rare, abnormally large grains by X-ray diffraction. *Journal of Materials Science* **2015**, *50*, 6719–6729.

(46) Gruber, J.; Lim, H.; Abdeljawad, F.; Foiles, S.; Tucker, G. Development of physically based atomistic microstructures: the effect on the mechanical response of polycrystals. *Computational Materials Science* **2017**, *128*, 29–36.

(47) Plimpton, S. Fast parallel algorithms for short-range molecular dynamics. *Journal of Computational Physics* **1995**, *117*, 1–19.

(48) Daw, M.; Foiles, S.; Baskes, M. The embedded-atom method: a review of theory and applications. *Materials Science Reports* **1993**, *9*, 251–310.

(49) Stukowski, A. Visualization and analysis of atomistic simulation data with OVITO – The Open Visualization Tool. *Modelling and Simulation in Materials Science and Engineering* **2009**, *18*, 015012.

(50) Ida, T.; Ando, M.; Toraya, H. Extended pseudo-Voigt function for approximating the Voigt profile. *Journal of Applied Crystallography* **2000**, *33*, 1311–1316.

(51) Uvarov, V.; Popov, I. Metrological characterization of X-ray diffraction methods at different acquisition geometries for determination of crystallite size in nano-scale materials. *Materials Characterization* **2013**, *85*, 111–123.

(52) Balzar, D. X-ray diffraction line broadening: Modeling and applications to high-T_c superconductors. *Journal of Research of the National Institute of Standards and Technology* **1993**, *98*, 321.

(53) Irfan, H.; M., R.; Anand, S. Microstructural evaluation of $CoAl_2O_4$ nanoparticles by Williamson–Hall and size–strain plot methods. *Journal of Asian Ceramic Societies* **2018**, *6*, 54–62.

(54) Stukowski, A.; Markmann, J.; Weissmüller, J.; Albe, K. Atomistic origin of microstrain broadening in diffraction data of nanocrystalline solids. *Acta Materialia* **2009**, *57*, 1648–1654.

(55) Derlet, P.; Van Petegem, S.; Van Swygenhoven, H. Calculation of x-ray spectra for nanocrystalline materials. *Physical Review B* **2005**, *71*, 024114.

(56) Balzar, D.; Popović, S. Reliability of the simplified integral-breadth methods in diffraction line-broadening analysis. *Journal of Applied Crystallography* **1996**, *29*, 16–23.

(57) Khatirkar, R.; Murty, B. Structural changes in iron powder during ball milling. *Materials Chemistry and Physics* **2010**, *123*, 247–253.

(58) Markmann, J.; Yamakov, V.; Weissmüller, J. Validating grain size analysis from X-ray line broadening: a virtual experiment. *Scripta Materialia* **2008**, *59*, 15–18.

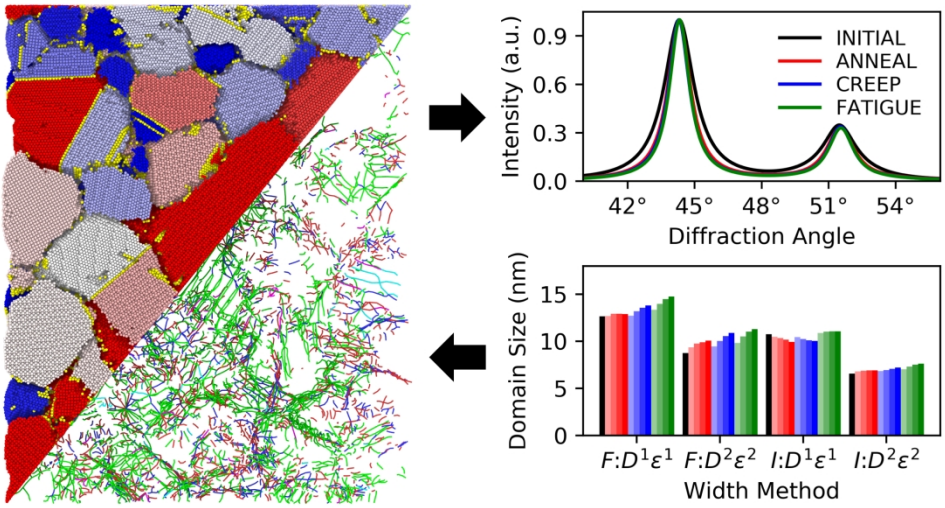
Intensity (a.u.)
0.9
0.6
0.3
0.0
INITIAL
ANNEAL
CREEP
FATIGUE
42°
45°
48°
51°
54°
Diffraction Angle
Domain Size (nm)
15
10
5
0
F:D1ε1
F:D2ε2
I:D1ε1
I:D2ε2
Width Method